Journal of Nanobiotechnology

RESEARCH Open Access

GAPDH-Silence Microsphere via Reprogramming Macrophage Metabolism and eradicating Bacteria for Diabetic infection bone regeneration

Jiale Jin[1†], Xiaowei Xia[2†], Chengxin Ruan[1†], Zhiyuan Luo[1], Yiqi Yang[1], Dongyu Wang[1], Yifang Qin[3], Dongdong Li[4], Yong Zhang[2*], Yihe Hu[1*] and Pengfei Lei[1*]

Abstract

Macrophage metabolism dysregulation, which is exacerbated by persistent stimulation in infectious and inflammatory diseases, such as diabetic infectious bone defects (DIBD), eventually leads to the failure of bone repair. Here, we have developed an injectable, macrophage-modulated GAPDH-Silence drug delivery system. This microsphere comprises chondroitin sulfate methacrylate (CM) and methacrylated gelatin (GM), while the dimethyl fumarate (DMF)-loaded liposome (D-lip) is encapsulated within the microsphere (CM@GM), named D-lip/CM@GM. Triggered by the over-expressed collagenase in DIBD, the microspheres degrade and release the encapsulated D-lip. D-lip could modulate metabolism by inhibiting GAPDH, which suppresses the over-activation of glycolysis, thus preventing the inflammatory response of macrophages in vitro. While beneficial for macrophages, D-lip/CM@GM is harmful to bacteria. GAPDH, while crucial for glycolysis of staphylococcal species (*S. aureus*), can be effectively countered by D-lip/CM@GM. We are utilizing existing drugs in innovative ways to target central metabolism for effective eradication of bacteria. In the DIBD model, our results confirmed that the D-lip/CM@GM enhanced bacteria clearance and reprogrammed dysregulated metabolism, thereby significantly improving bone regeneration. In conclusion, this GAPDH-Silence microsphere system may provide a viable strategy to promote diabetic infection bone regeneration.

Keywords Diabetic infection bone defect, Dimethyl fumarate, Microsphere, Macrophage metabolism

[†]Jiale Jin, Xiaowei Xia and Chengxin Ruan contributed equally to this work.

*Correspondence:
Yong Zhang
zhangy6658@163.com
Yihe Hu
xy_huyh@163.com
Pengfei Lei
leipengfei@zju.edu.cn

[1]Department of Orthopedic Surgery, The First Affiliated Hospital, Zhejiang University School of Medicine, Hangzhou 310003, China
[2]Department of Orthopaedics, The First Affiliated Hospital of Soochow University, Soochow University, Suzhou 215006, China
[3]Department of Endocrinology, The Children's Hospital, School of Medicine, Zhejiang University, Hangzhou 310052, China
[4]Department of Orthopedic Surgery, Ningxia Medical University, Yinchuan 200233, China

Introduction

Diabetic infectious bone defects (DIBD) represent a significant medical challenge, leading to high disability and mortality [1, 2]. Considering aging populations and rising diabetes incidence, combined with the growing threat of antibiotic-resistant bacteria, the occurrence rate of these diseases is escalating [3]. Autogenous bone grafting is regarded as the gold standard in traditional bone defect treatments [4]. However, this treatment is inadequate for the complex microenvironment of DIBD, notably immune cell metabolic dysregulation and chronic infection. Long-term hyperglycemia induces cellular dysfunction and chronic damage, disrupting metabolic balance [5]. This shift frequently results in enhancing glycolysis, impacting macrophage functionality, promoting inflammation, and hindering tissue repair [6]. Additionally, hyperglycemia also provides a conducive environment for pathogenic bacterial growth, inhibiting bone remodeling [7]. Currently, conventional treatment strategies involve combining biomaterials with antimicrobials, such as antibiotics [8], metallic nanoparticles [9], antimicrobial peptides [10], and biological extracts [11]. Despite persistent metabolic imbalance post-bacterial infections, the need to reshape dysregulated immune cell metabolism is frequently overlooked, leading to adverse outcomes [12]. This persistent inflammatory stress environment not only suppresses bone tissue repair but also contributes to immune system exhaustion, which may lead to the infection recurrence [13, 14]. Consequently, the urgent priority is to develop a safe, efficient, and comprehensive therapeutic strategy that reprograms macrophage metabolism and bacteria clearance to combat DIBD.

Dimethyl fumarate (DMF), a derivative of fumarate, is an intermediate in the tricarboxylic acid cycle. DMF has been found to target Glyceraldehyde 3-phosphate dehydrogenase (GAPDH) and inactivates its enzyme activity in both mice and humans [15]. GAPDH, as an essential part of glycolysis, its inhibition downregulates glycolysis in myeloid and lymphoid cells, shifting to oxidative phosphorylation and preventing immune activation [16, 17]. However, this inhibitory effect of GAPDH was also found to work on bacteria, which is lethal to Staphylococcus aureus (*S. aureus*) [12]. This inhibition, on one hand, helps to reprogram of the metabolism in macrophage, on the other hand, may also destroy energy metabolism in bacteria. Furthermore, this represents a novel application for an established medication: DMF, introduced to the US market in March 2013 and approved in the European Union for treating psoriasis and multiple sclerosis, has significantly reduced the time and costs associated with drug research and development [18].

Due to adverse reactions with systemic injection, topical use of DMF is preferred [19]. However, DMF can rapidly diffuse and be easily deactivated, resulting in a short duration of action in the diabetic infection microenvironment. Consequently, a sustainable drug-eluting system is urgently needed. Recently, microspheres have emerged as an attractive drug-delivery platform due to their excellent biocompatibility and controllable drug release capabilities. Our research group has previously developed arbutin-modified microspheres for treating osteoarthritis [20]. Addressing the specific needs of DIBD, we incorporated gelatin methacrylate (GM) hydrogel into our new system, it can be degraded by collagenase secreted by proinflammatory macrophages and bacteria [21, 22]. Furthermore, we used chondroitin sulfate methacrylate (CM), which imparts photo-crosslinking ability. Chondroitin sulfate, a significant structural component of connective tissue and cartilage, encompasses anti-inflammatory, antioxidant, and enzymatic regulatory properties [23]. With its ability to conjugate both covalently and non-covalently due to its modifiable groups and active functional groups, chondroitin sulfate is recognized as a potential contender in hydrogel networks [24]. In addition, chondroitin sulfate can target CD44 on the surface of inflammation- activated macrophages [25, 26]. With GM and CM as the basis, we have the potential to develop a new drug delivery platform with inflammatory response and macrophage targeting features. Moreover, liposomes (lip) act as slow-release reservoirs, prolonging drug exposure.

In this work, DMF-loaded liposomes (D-lip) were incorporated into the CM@GM hydrogels through non-covalent interactions, creating the injectable GAPDH-Silence microspheres capable of clearing bacteria and correcting dysregulated metabolism (Fig. 1). Furthermore, this collagenase-sensitive hydrogel enables controlled release of D-lip upon infection, exhibiting effective antibacterial properties in vitro. Additionally, the D-lip/CM@GM can inhibit the key glycolysis enzyme GAPDH in macrophages, further affecting the expression of downstream inflammation-related pathways. In the DIBD rat model, it demonstrated antibacterial, immune-regulatory, and bone repair-promoting functionalities. The GAPDH-Silence microspheres exhibit significant therapeutic potential for treating infectious and inflammatory diseases, including diabetes-related bone defects.

Materials and methods

Preparation of microspheres

The microfluidic syringe pump was used to form a microfluidic device through a silicone hose together with two separate syringes and a three-way connector. The external phase was used as the continuous phase using Span 80 (Macklin, shanghai, China) configured with isopropyl myristate (Macklin) (1:4 v/v). CM (Engineering For Life, China) and GM (Engineering For Life, China) solutions, mixed with photoinitiators at a concentration of

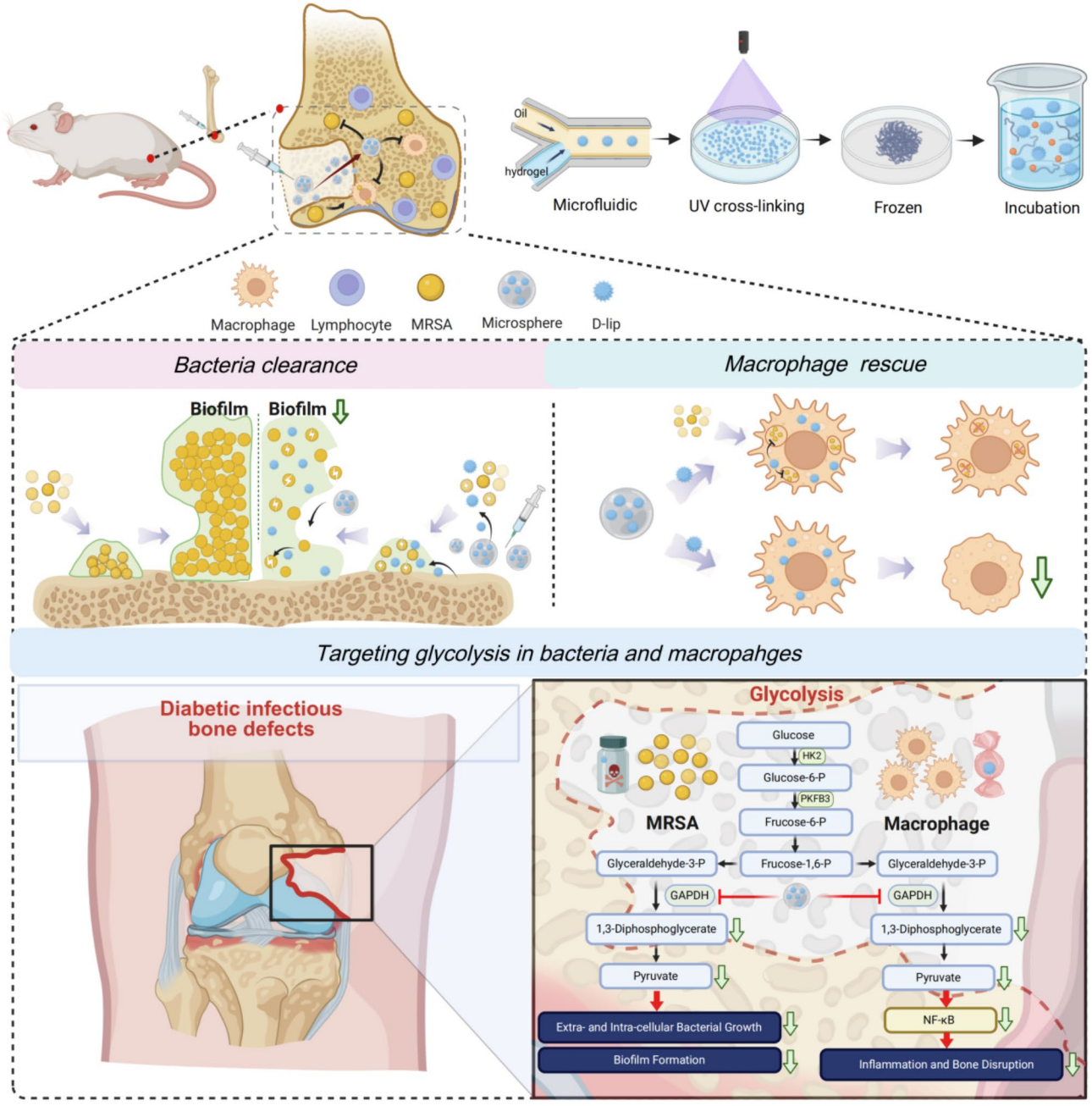

Fig. 1 Schematic diagram of the GAPDH-Silence microsphere system for antibacterial and macrophage metabolic reprogramming. The D-lip/CM@GM microsphere was designed via microfluidic. Responding to over-expressed collagenase in diabetic infectious bone defects (DIBD), the microspheres decompose and release the encapsulated D-lip. D-lip could modulate metabolism by inhibiting GAPDH, which suppresses the over-activation of glycolysis, thus preventing the inflammatory response. Conversely, D-lip/CM@GM also manages to hinder glycolysis in Methicillin-resistant Staphylococcus aureus (MRSA), thereby contributing to the eradication of the bacteria. Ultimately, the D-lip/CM@GM system facilitates the repair of diabetic infectious bone defects

10%, were used as the dispersed phase. Among them, four microspheres with GM: CM mass ratios of 1:4, 1:2, 1:1 and 2:1 were prepared according to the different masses of GM and CM. The aqueous and oil phases were uniformly pushed into the three-way connector through a syringe and photocross-linked under UV light irradiation to cure the microspheres. The collected four microspheres were washed repeatedly with 75% ethanol to remove the continuous phase. The microspheres were then soaked in fresh PBS for 4 h and repeated 3 times to remove other additives. To obtain porous microspheres, the purified microspheres were frozen at -80 °C for 4 h and then freeze-dried for 48 h.

Characterization of Microspheres

(i) The morphology and size of the microspheres were observed under an optical microscope (CX23, Olympus, Japan) and bright field images of the microspheres were taken to determine the particle size of each group of microspheres using Image J. (ii) After spraying the microspheres with gold, the size of the lyophilized microspheres and the pore size on the microsphere surface were characterized using a scanning electron microscope (SEM, SU8100, Hitachi, Japan). (iii) The surface elements of the samples were photographed by energy dispersive spectroscopy (EDS, EDAX, USA). The structure of the prepared microspheres was analyzed using a Fourier transform infrared spectrometer (FTIR, Nicolet iS50, Thermo Fisher Scientific), thin slices were prepared from potassium bromide abrasive flakes and scanned in the range of 400–4000 cm^{-1} at 4 cm^{-1} resolution 128 times. (iv) An X-ray photoelectron spectrometer (XPS, ESCALAB 250Xi, Thermo Fisher Scientific) was used to test the changes of elements on the surface of the microspheres. The test pass energy (Passing-Energy) was 30 eV in steps of 0.05 eV and charge correction was performed using C1s=284.80 eV binding energy as an energy standard.

Biocompatibility Measurement

To assess the adhesion and proliferation ability of microspheres to cells, bone marrow mesenchymal stem cells (BMSCs) were co-cultured with different groups of microspheres for one week, and subsequently photographed under a light microscope to observe cell adhesion and proliferation.

To assess the biotoxicity of microspheres, live/dead cell viability assay was performed by Live/Dead staining kit (Beyotime, Shanghai, China) according to the manufacturer's instructions. After co-culturing BMSCs with different groups of microspheres for 1, 3 and 5 d, the cell-loaded microspheres were stained with live/dead working solution for 30 min at room temperature. The stained cells on the microspheres were observed and photographed under a fluorescence microscope (Zeiss Axiovert 200; Carl Zeiss Inc., USA).

Degradation experiment

To evaluate the degradation ability of the microspheres in different environments, 50 mg of the samples were added to 1 mL of PBS solution and 1 mL of PBS containing collagenase at a concentration of 5 U/mL, respectively, and placed in a shaker (37 °C, 120 rpm). The supernatant was changed daily to maintain enzyme activity. At predetermined time points, the morphology of the microspheres after degradation was observed and photographed under the light microscope, and the microspheres were collected and washed several times with sterile deionized water. The microspheres were lyophilized, weighed and the degradation rate was calculated according to the following formula:

$$\mathrm{DP}\,(\%) = \frac{\mathrm{W_0} - \mathrm{W_t}}{\mathrm{W_0}} \times\ 100\%$$

where W_0 is the weight of the initial lyophilized sample, and W_t is the weight of the lyophilized sample after time t.

To visualize the results even more, the microspheres were stained red using hydrogel dye, and microspheres (50 mg) were immersed in equal volumes of PBS and collagenase-containing PBS (5 U/mL) in glass vials and photographed at specific times.

Response release capability of CM@GM

BSA has been used as a model protein for assessing release capacity because of its stability, lack of effect in many biochemical reactions, and low cost. Four sets of microspheres spiked with BSA were prepared by immersing each microspheres (100 mg) in PBS (4 mL) and PBS containing collagenase at a concentration of 5 U/mL (4 mL) and placed in a shaker at 37 ℃. The release efficiency was calculated by aspirating each release solution (100 μL) at predetermined times and determining the protein concentration using the BCA method. The supernatant was changed daily to maintain enzyme activity.

Preparation of lip and D-lip

Lip were prepared by a thin-film dispersion method. Briefly, lecithin (Yuanye Bio-Technology, Shanghai, China), cholesterol (Aladdin, Shanghai, China), and octadecylamine (Aladdin) (80:40:4, w/w/w) were dissolved in chloroform and evaporated at 60 °C for 30 min. The dried lipid membranes were then combined and sonicated with deionized water for 20 min to obtain dispersed multilayer liposomes. Subsequent filtration was carried out using 0.45 μm and 0.22 μm pore filters (Sorfa, Zhejiang, China) to progressively extrude out and reduce the size of the liposomes. D-lip were prepared with lecithin, cholesterol, octadecylamine and DMF (80:40:4:4, w/w/w/w).

Characterization of lip and D-lip

Transmission electron microscopy (TEM, FEI Talos F200X, USA) was applied to observe the structure of NPs. The particle size and zeta potential of lip NPs and D-lip NPs were tested by a particle size and zeta potential analyzer (Malvern Zetasizer Nano ZS90, United Kingdom). Particle size distributions, zeta potentials, drug encapsulation capacity, and loading capacity were analyzed and calculated. In order to test the encapsulation efficiency (EE) and loading capacity (LC) of DMF by liposomes, it was tested by ultraviolet-visible spectrophotometer

(TU-1900, Beijing, China). The DMF standard curve was plotted based on the peak UV spectra of different concentrations of DMF, the EE and LC of DMF in D-lip NPs was calculated by the following equation:

$$\text{Loading capacity (LC)} = \frac{(W_T - W_F)}{W_{NP}} \times 100\%$$

where W_T is the total weight of DMF, W_F is the weight of nonencapsulated free DMF, and W_{NP} is the weight of lipo@DMF.

$$\text{Encapsulation efficiency (EE)} = \frac{(W_T - W_F)}{W_T} \times 100 \text{ percent}$$

where W_T is the total weight of DMF, and W_F is the weight of nonencapsulated free DMF.

Preparation of D-lip/CM@GM

The prepared CM@GM microspheres were mixed with the prepared D-lip at room temperature and placed on a shaker for 4 h. Subsequently then freeze-dried for 48 h.

Characterization of D-lip/CM@GM

TEM was applied to observe the structure of D-lip/CM@GM. For test the drug release, the D-lip/CM@GM (100 mg) were prepared by immersing in PBS (4 mL) and PBS (4 mL, containing collagenase) and placed in a shaker at 37 °C. The amount of DMF released from D-lip/CM@GM was measured by ultraviolet-visible spectrophotometer and calculated based on a previous standard curve of DMF concentration. In addition, take degradation pictures of D-lip/CM@GM and CM@GM.

Macrophage culture and cell viability

The Raw 264.7 cell line obtained from ATCC was maintained in high-glucose DMEM medium with 10% fetal bovine serum. To assess cell viability after treatment with microspheres at different time, a CCK-8 assay (Dojindo, Japan) and Calcein AM/PI Double Stain Kit (Solarbio, China) were performed following the provided protocol.

Immunofluorescence staining (IF)

The specimens were initially treated with a 4% paraformaldehyde solution (Solarbio, China) for fixation, followed by permeabilization using IF blocking solution (Beyotime, China) for 15 min. Subsequently, the samples were incubated with the specific primary antibodies at 4 °C overnight. On the following day, secondary Alexa 488- or Alexa 555-labeled antibodies were applied to the samples and incubated at room temperature for 40 min. Finally, the specimens were visualized using a Confocal microscope (Leica STELLARIS5, Germany).

Bacterial strains and antibacterial experiments

Methicillin-resistant Staphylococcus aureus (MRSA) was cultured in tryptic soy broth (TSB) at 37 °C overnight. For evaluation of antibacterial efficacy, different hydrogel groups were submerged in 1 mL of bacterial suspension (1×10^6 CFUs/mL) at 37 °C for 2 h. Following incubation, the samples were extracted, and the supernatant was obtained and diluted with 100x PBS. Subsequently, 100 μL of the solution was spread on Blood Agar plates and incubated at 37 °C overnight, after which the number of colonies was enumerated.

The Live/Dead BacLightTM bacterial viability kits (Invitrogen, USA) were employed for assessing the antibacterial efficacy of the hydrogels. The diluted bacterial solution (100 μL) was incubated with SYTO 9 and propidium iodide (PI) for 60 min in the absence of light. The ratio of live to dead bacteria was then semi-quantitatively determined using ImageJ (V1.8.0, USA) based on the fluorescence intensity of SYTO 9 and PI.

The bacterial suspension was then transferred to a tube and centrifuged. Subsequently, the samples were fixed first in 2.5% glutaraldehyde solution at 4 °C for 2 h, followed by fixation in 1% osmium tetroxide for an additional 2 h. The samples were then dehydrated using a series of ethanol solutions. Following further processing for penetration and embedding, ultra-thin sections were obtained using a microtome. Finally, the sample sections were stained with citric acid and uranyl acetate for 10 min before observation under TEM.

To examine the 3D structure of the biofilm, it was cultivated on the discs in confocal dishes. Subsequently, a LIVE/DEAD BacLight bacterial viability kit was utilized, and the biofilm was observed using a confocal microscope.

To assess intracellular bacterial clearance in vitro, green fluorescent protein (GFP)-tagged MRSA was co-cultivated with macrophages at a ratio of 10:1 for 24 h, and observed the fluorescence within macrophages using confocal microscopy to evaluate intracellular bacterial killing.

Flow cytometry

Macrophages were cultured with various sample groups for a 3-day incubation period. Flow cytometry was employed to evaluate the expression levels of iNOS and Arg-1, markers for M1 and M2 macrophages, respectively. Anti-mouse antibody probes were utilized for immunophenotyping analysis. Data acquisition was performed using the BD LSR Fortessa analyzer with FACSDIVA software (Beckton Dickinson, USA), and subsequent analysis was conducted using FlowJo 10.0 software.

RNA extraction and RT-PCR

Total RNA was extracted from macrophages using the TRIzol reagent (Accurate Biology, China) and subsequently reverse-transcribed into cDNA (Accurate Biotechnology, China). The RT-PCR reaction conditions were as follows: 95 °C for 10 min; 40 cycles of 95 °C for 15 s and 60 °C for 60 s. RT-PCR was carried out using a CFX96 RT-PCR System (Bio-Rad, USA). The mRNA levels of the target gene were quantified using the $2^{-\Delta\Delta Ct}$ method and normalized to β-actin expression.

Western blotting

The samples were lysed with RIPA buffer, which included protease and phosphatase inhibitors (Beyotime, China). A BCA protein assay kit (Solarbio, China) was used to measure the protein concentration. Equal amounts of protein were then applied to a 10% SDS-PAGE gel and transferred to polyvinylidene fluoride membranes (Millipore, USA). The membranes were blocked using Protein-Free Fast Blocking Buffer (Solarbio, China) and probed with primary antibodies overnight at 4 ℃. Secondary antibodies were applied afterward. The immunoreactive bands were analyzed with Image-J.

GAPDH activity ana lactate analysis

GAPDH activity was measured with a GAPDH activity kit (Abcam, USA). Cell and bacteria were homogenized in GAPDH assay buffer, and enzyme activity was assessed in a 96-well plate following the kit instructions. Absorbance was read at 450 nm in kinetic mode at 37 °C. GAPDH activity was calculated per the kit protocol. Lysate protein quantification was done using the standard BCA Kit (Thermo Fisher Scientific, USA), and results were presented as U/mg of total protein. The concentration of lactate (diluted 1:50 with assay buffer) was quantified following the manufacturer's guidelines of the Lactate-Glo™ Assay kit (Promega Corporation, USA).

Extracellular acidification rate (ECAR) and oxygen consumption rate (OCR)

An intraperitoneal injection of STZ in rats aged 8 weeks produced a diabetic model. Macrophages derived from bone marrow were obtained from diabetic SD rats. The femurs and tibias were sterilely harvested, and the bone marrow was extracted using α-MEM (Thermo Fisher Scientific, USA). After removing the red blood cells with lysis buffer, the bone marrow cells were gathered and rinsed in α-MEM. These cells were cultured in 100 mm dishes containing α-MEM with 10% fetal bovine serum (FBS), 1% penicillin-streptomycin (P/S), and 10 ng/ml macrophage colony-stimulating factor (MCSF, Peprotech, USA) for one day at 37 °C in a 5% CO_2 humidified environment. On the second day, non-adherent cells were retrieved, washed in PBS, and then cultured in α-MEM enriched with 10% FBS, 1% P/S, and 30 ng/ml MCSF for four additional days.

Using the Seahorse XFe 96 Extracellular Flux Analyzer, measurements of ECAR and OCR were conducted. Cells were seeded in the microplate. Subsequently, the cells underwent a series of treatments including exposure to glucose, oligomycin, and 2-DG to determine ECAR levels. Following this, the cells were subjected to oligomycin (1 μM), a reversible oxidative phosphorylation inhibitor (FCCP), and rotenone/antimycin (A & R). The obtained results, expressing OCR in picomoles per minute and ECAR in mpH, were analyzed using the Seahorse XF-96 Wave software.

Animal experiments

The antibacterial, immunomodulatory, and osteogenesis capabilities of microspheres were assessed in STZ-induced diabetic rats. Each rat was anesthetized via intra-abdominal injection with 3% pentobarbital sodium, followed by surgical exposure of both distal femurs. A 2 mm hole was precisely drilled into each femur, followed by injecting a diluted MRSA suspension (10 μl per hole, with a concentration of 1×10^8 CFU/ml). Various hydrogel formulations were then implanted into these holes. After four weeks, the rats were euthanized, and their femurs were extracted for colony culture, micro-CT, and histological evaluations to assess the efficacy of hydrogels in vivo. The rat experiment received ethical approval from the Animal Experimental Ethical Inspection of the First Affiliated Hospital, Zhejiang University School of Medicine, with the approval number 2024sydw1252.

Peripheral femur samples of the rats were collected and immersed in 2 ml PBS. The homogenate was then evenly smeared on blood agar plates and subjected to CFU counting after overnight incubation. For the micro-CT scan, the samples were secured in a 4% paraformaldehyde (PFA) solution at 37 °C under gentle agitation for two days. High-resolution Micro-CT images of all specimens were obtained using a device from Milabs in the Netherlands. The new bone surface area of all samples was determined using ImageJ software and normalized to the original defect area. Bone volumetric density (BV/TV%) was analyzed using the SkyScan CT-Analyzer program (Bruker, Germany).

After micro-CT scanning, fixed tissues were immersed in EDTA decalcifying solution at 37 °C under gentle agitation for four weeks. Post-decalcification, the samples were embedded in paraffin and sectioned into slices. H&E was performed to assess inflammation, with stained results inspected via an inverted fluorescence microscope (Olympus IX73, Japan). During the deparaffinizing of tissue slices, Tris-EDTA solution (Solarbio, China) was applied at 65 °C for four hours, followed by a 30-minute blocking step using IF blocking solution (Solarbio,

China). The corresponding primary antibodies were incubated overnight at 4 °C, then bound with matching fluorescent secondary antibodies for staining. Results were observed using a laser confocal microscope (Olympus FV3000, Japan). Immunohistochemical experiments were conducted following the instructions in the immunohistochemical kit (ZSGB-Bio, China).

Molecular docking analysis

To assess the binding affinities and interaction patterns between the DMF and GAPDH, we utilized Autodock Vina 1.2.2, a computational tool for protein-ligand docking. The chemical structure of ENMD-2076 was sourced from PubChem Compound (https://pubchem.ncbi.nlm.nih.gov/) [27]. The three-dimensional structures of KDR (PDB ID, 5EW3; resolution, 2.5 Å) and BIRC5 (PDB ID, 4AOI; resolution, 1.9 Å) were obtained from the Protein Data Bank (http://www.rcsb.org/pdb/home/home.do). In preparation for docking, all proteins and molecular data were transformed into PDBQT format, with the removal of water molecules and addition of polar hydrogen atoms. The docking grid box was designed to encapsulate the active site of each protein, ensuring space for unrestricted molecular motion. The dimensions of the grid box were established at 30 Å × 30 Å × 30 Å with a grid point spacing of 0.05 nm. Docking simulations were conducted using Autodock Vina 1.2.2 (http://autodock.scripps.edu/).

Statistical analysis

Each experiment was conducted a minimum of three times, and the data is reported as means ± SD. The statistical significance among the sample groups was evaluated using t-test, one-way analysis of variance (ANOVA) and two-way ANOVA, with a P value of less than 0.05 considered as statistically significant.

Results and discussions

Characterization of CM@GM

In this study, we designed a responsive microsphere drug-carrying system based on GM and CM for DIBD, and four types of microspheres with different mass ratios were synthesized by a microfluidic platform. Light microscopy revealed that the non-freeze-dried microspheres displayed smooth morphology, uniform sizes, and consistent particle sizes across all mass ratio groups (Fig. 2A and S1A). SEM results showed that the pore size of the microspheres narrowed or even disappeared with the increase in the mass ratio of GM, suggesting that the different mass ratios had a greater effect on the loose porous structure of the microspheres, which might be related to the increase in the cross-linking density as well as the interaction between the polymer chains [28, 29], whereas the microspheres with mass ratio of 1:1 showed a more stable loose porous structure (Fig. 2B). With an increased mass share of CM, the concentration of elemental S increased, reflecting successful GM and CM cross-linking in the microspheres, as evidenced by the narrow elemental S spectrum in high-resolution XPS (Fig. S1C). The results of FTIR showed (Fig. S1B) that a wider spectral band was observed near 3289 cm^{-1}, which was attributed to the stretching of -OH and N-H of GM. The amide bands present in GM indicate different vibrational states of the peptide bond. The vibration associated with the N-H bond (which is also a part of the C-N bond) is called amide I, occuring at 1236 cm^{-1}, and the peak at 1533 cm^{-1} is called amide II, which is associated with the N-H bond. The vibrational peak at 1633 cm^{-1} is called amide III, showing the vibration of C = O bond [30]. In addition, CM contains characteristic sulfate bonds [31]. The peak at 842 cm^{-1} is attributed to C-S-O vibration while the peak at 1255 cm^{-1} shows S = O vibration [32].

Functional validation of CM@GM

As an injectable drug delivery system, it needs to be biocompatible and capable of promoting cell adhesion and proliferation [32]. Light microscopy results indicated that the functionalized microspheres promoted adhesion and proliferation of BMSCs (Fig. 2 C, E). In addition, we characterized the cytocompatibility of CM@GM microspheres with different mass by Live/Dead staining. The viability of BMSCs co-cultured with different mass ratios of CM@GM microspheres for 1, 3, and 5 days was examined by Live/Dead staining assay (Fig. 2D). Apparently, dead cells (red staining) were hardly observed in all groups, while live cells (green staining) showed good viability at all time points. Notably, cell density gradually increased with culture time, which was further confirmed by quantitative assessment of live cells (Fig. 2F). These cellular findings demonstrate that CM@GM microspheres exhibit excellent biocompatibility and are free of cytotoxicity, which is a prerequisite for in vivo experiments and clinical applications.

CM@GM microspheres act as an effective carrier, preventing rapid drug loss and enabling responsive localized drug release. To demonstrate the great responsiveness of CM@GM microspheres, we simulated the DIBD environment in vitro using collagenase and verified it by detecting the degradation of microspheres as well as drug release experiments. The degradation curves showed (Fig. S2A) that the four microspheres degraded faster in the collagenase environment than in PBS, suggesting that the drug-carrying system was responsive to the inflammatory environment. Particularly, CM@GM microspheres

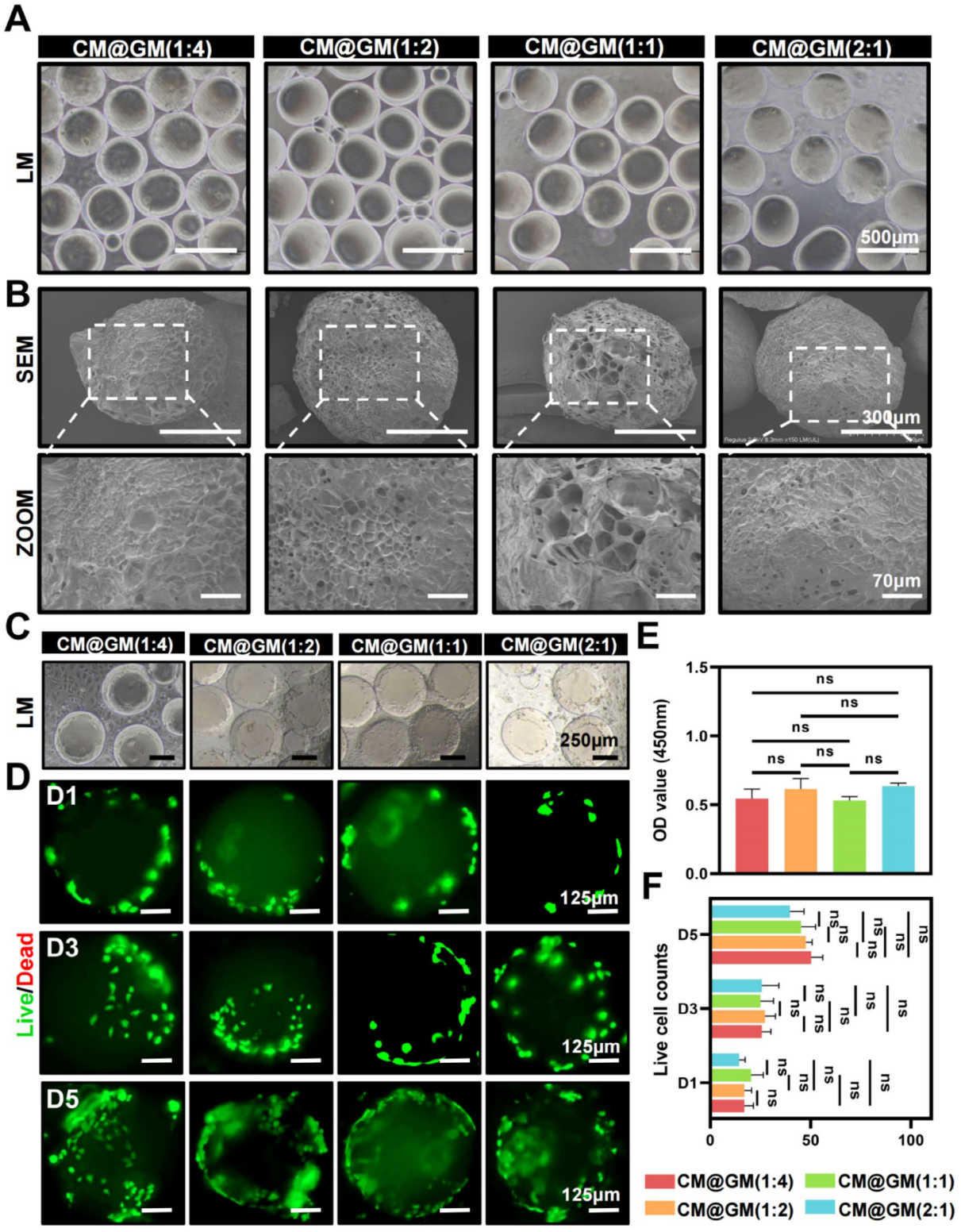

Fig. 2 Preparation and Characterization of CM@GM. (**A**). Light microscopy (LM) results of non-freeze-dried different mass ratios CM@GM microspheres. (**B**). Representative scanning electron microscopy (SEM) images and corresponding high magnification images of different microspheres. (**C**). Light microscopy (LM) results of adhesion and proliferation of different microspheres after one week of co-culture with cells (Day 7). (**D**). Representative Live/dead staining of cells in different groups at Day 1, Day 3, and Day 5. (**E**). CCK-8 experiment for cells in different groups. (**F**). Quantitative analysis of live cell counts in the different treatment groups. $n = 3$, The values represent mean ± SD. Statistically, significant differences are indicated ns where $p \geq 0.05$, * where $p < 0.05$, ** where $p < 0.01$, *** where $p < 0.001$, and **** where $p < 0.0001$ between the indicated groups

with a 1:1 mass ratio degraded faster, likely due to their sparser porous structure which reduces the crosslink density of the hydrogel microspheres upon hydrolytic degradation, allowing more solution to permeate [33], resulting in better responsiveness. Similarly, the drug release profile showed that 1:1 microspheres had better drug release properties in the inflammatory environment (Fig. S2B).

Given that the 1:1 CM@GM microspheres have a well-stabilized loose porous structure as well as good inflammatory responsiveness, we selected them for subsequent experiments. Energy dispersive X-ray spectroscopy (EDS) confirmed the homogeneous distribution of the elements C, N, O, and S on the microspheres (Fig. S3A), further validating the successful construction of the CM@GM microspheres. For further validation, we stained the microspheres to visualize degradation. After 2 weeks of incubation, all collagenase-free microspheres were stable and only slightly hydrolyzed, whereas the microspheres exhibited continuous biodegradability in the presence of collagenase (Fig. S3B).

Characterization of D-lip/CM@GM

Next, we further constructed the drug-carrying system. The lip and D-lip were prepared by thin-film dispersion method, and TEM showed that lip and D-lip had regular spherical morphology (Fig. S3C). Size and zeta potential analyses revealed that the average diameters of lip and lip@DMF, respectively, were 225.03 ± 6.58 nm and 223.07 ± 5.01 nm (Fig. S3D). There was no significant difference in the size of the nanoparticles after DMF encapsulation. The average zeta potential values of the above two nanoparticles were − 45.7 ± 1.20 mV and − 42.1 ± 0.26 mV, respectively (Fig. S3E). In addition, the encapsulation rate of D-lip NPs was calculated to be 82.5 ± 1.68% and the drug loading rate was 3.57 ± 0.33%. Liposomal encapsulation provides slow and sustained release of DMF [34, 35]. The release profile shows that the cumulative release profile of DMF loaded in lip is biphasic, with a rapid release period followed by a slower release period (Fig. S3G). In addition, the incorporation of lip into CM@GM could further improve the stability of the drug delivery system and achieve responsive drug delivery (Fig. 3A). TEM results showed that lipo@DMF was combined with CM@GM microspheres (Fig. 3B), and the EDS results also showed that the drug-loaded liposomes were uniformly distributed on the microspheres (Fig. 3D). Also the release profiles of D-lip/CM@GM in different environments again showed that can be used as an effective drug delivery system to control drug responsive release (Fig. 3 C). Moreover, the results of microscopic images of degradation were consistent (Fig. S4A). Also, in vivo studies were conducted to determine the biosafety of D-lip/CM@GM (Fig. S5A). Overall, our designed microsphere drug delivery system is biocompatible and inflammation-responsive, making it an ideal carrier for in vivo therapeutic applications.

Metabolic reprogramming of D-lip/CM@GM in vitro

Immune cells play a crucial role in host defense against infections and cancer. Upon encountering threat signals, immune cells are activated, modulating their immune functions. However, studies showed that metabolically active immune cells exhibit express metabolic changes which are further reiterated upon activation [36]. Therefore, regulating immune cell metabolism could serve as a significant intervention method in treating inflammation-related diseases [37]. Elevated insulin, fatty acids, glucose, and cholesterol levels lead to a metabolic pathway discordance in diabetics, which results in an immune cell function imbalance, increasing glucose uptake and glycolytic metabolism, while promoting an inflammatory state [38]. By reanalyzing GEO datasets for macrophages under diabetic conditions (GSE164338), gene expression profiles of diabetic and normal conditions were compared (Fig. 4A). We found that increasing expression of genes involved in glycolysis (as per Kyoto Encyclopedia of Genes and Genomes M00001) in diabetic patients [39], with significant alterations observed in GAPDH, GCK, and ENO3 (Fig. 4B). Western blot further confirmed the upregulation of GAPDH expression in diabetic macrophages (Figure. S6A, B). These findings support the feasibility of immune metabolism treatment. Previous studies found that DMF inactivates the cysteine catalytic site of GAPDH. Molecular docking experiments further indicated a high affinity between DMF and GAPDH (Fig. 4 C). GAPDH, often referred to as a housekeeping gene, functions indispensably in glycolysis and gluconeogenesis [40]. It steps up as a rate-limiting enzyme regulating the rate of aerobic glycolysis when macrophages are activated [17]. Interestingly, in an inflamed state, a GAPDH-specific blockade can be induced through D-lip treatment, manifested as a decrease in GAPDH activity (Fig. 4D, E). To further discover the impact of D-lip/CM@GM on glucose metabolism, our evaluation focused on glycolysis and mitochondrial metabolism in macrophages. The findings showed an increase in the extracellular acidification rate (ECAR) and a decrease in the oxygen consumption rate (OCR) of macrophages under the effect of D-lip/CM@GM. These results provided evidence for inhibiting GAPDH activity and downregulating glycolysis mediated by D-lip/CM@GM, where a blockage in glycolysis occurs within GAPDH (Fig. 4F).

We next explored whether the immunological effects induced by D-lip/CM@GM were mediated through

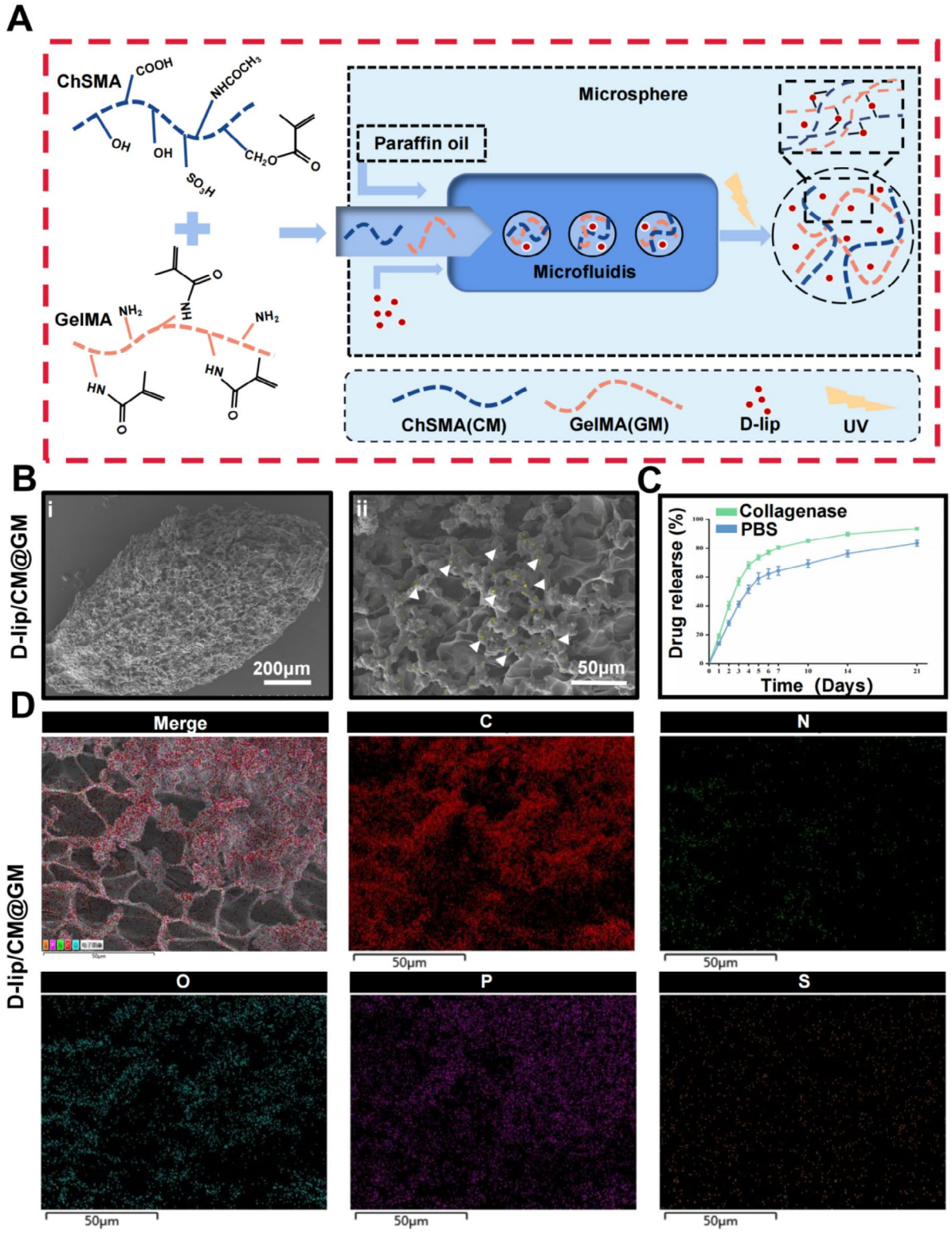

Fig. 3 Preparation and Characterization of D-lip/CM@GM. (**A**). Schematic diagram of preparing GAPDH-Silence microsphere system. The microsphere is composed of Chondroitin Sulfate Methacrylate (CM) and Methacrylated Gelatin (GM), encapsulating a Dimethyl Fumarate (DMF)-loaded liposome (D-lip). (**B**). Representative SEM images and corresponding high magnification images of D-lip/CM@GM, D-lip was labeled by white triangle. (**C**). Drug release profiles from D-lip/CM@GM microspheres in different environments within 3 weeks. (**D**). Representative Energy dispersive X-ray spectroscopy (EDS) image of the elements C, N, O, P, and S in the D-lip/CM@GM

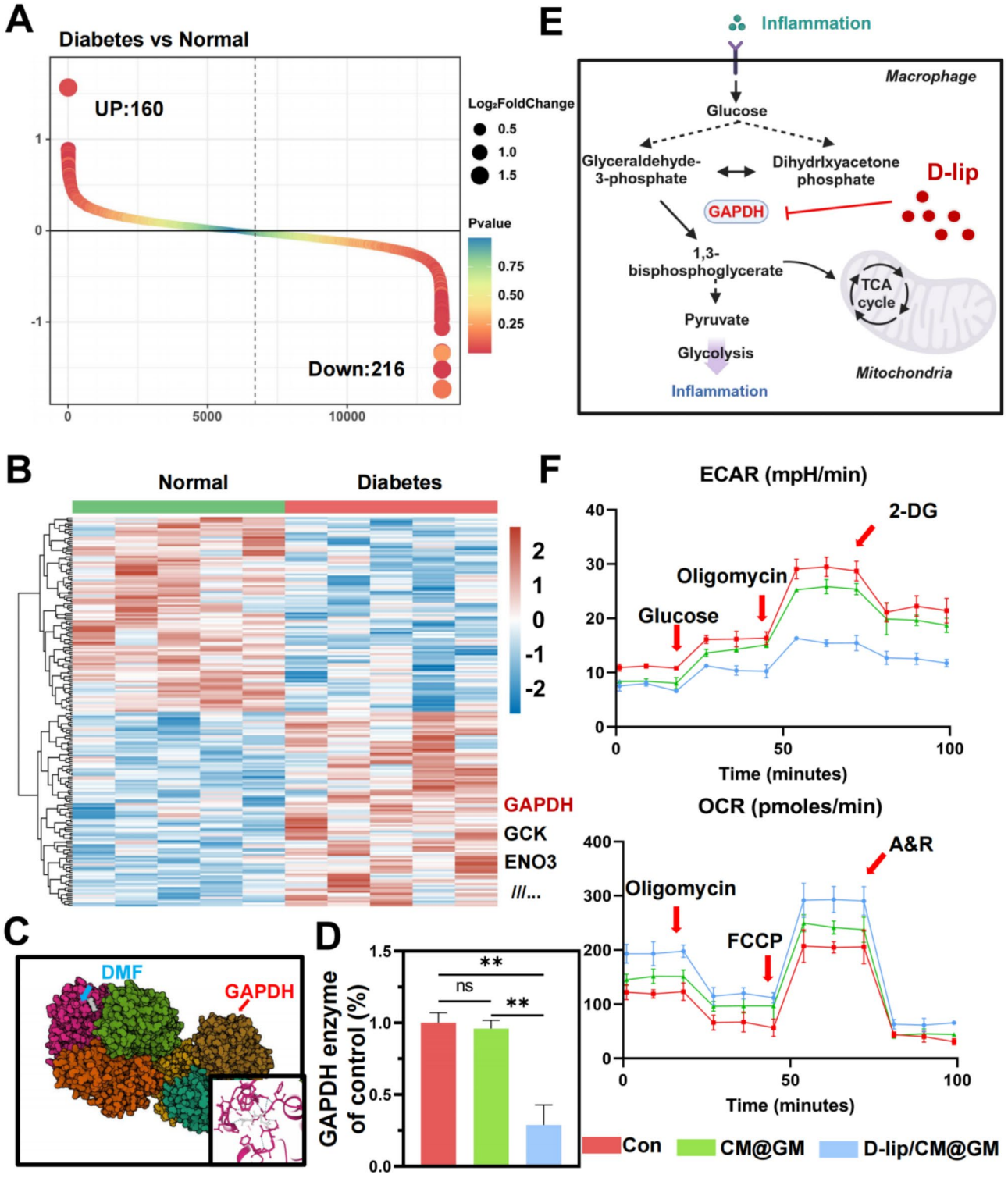

Fig. 4 Metabolic reprogramming of D-lip/CM@GM in macrophages. (**A**). Image of RNA expression ranking in the macrophages of diabetes and normal. 160 genes were upregulated and 216 genes were downregulated. (**B**). The heatmap of RNA levels in macrophage of normal (Green) and diabetes (Red). GAPDH is highly expressed and highlighted. (**C**). Molecular docking analysis between DMF and GAPDH. (**D**). Semi-quantitative analysis of GAPDH enzyme activity compared to the control (Con) group. (**E**). Effects of D-lip/CM@GM on the ECAR and OCR in macrophages. 2-DG (2-deoxy-d-glucose). FCCP (carbonyl cyanide-4 (trifluoromethoxy) phenylhydrazone). A&R (antimycin/rotenone). The values represent the mean ± SD. Statistically significant differences are indicated as ns where $p \geq 0.05$, * where $p < 0.05$, ** where $p < 0.01$, *** where $p < 0.001$, and **** where $p < 0.0001$ between the indicated groups

GAPDH inhibition and aerobic glycolysis in an LPS-induced inflammation model. Initially, we studied the impact of D-lip/CM@GM on the classical macrophage activation. The observation that D-lip/CM@GM significantly inhibited the expression of induced nitric oxide synthase (iNOS) and increased Arginase-1 (Arg-1) protein levels in macrophages, demonstrated its capability to prevent macrophages from activating (Fig. 5A, B). Flow cytometry showed a decrease in the proportion of the classically activated macrophages (CD11b+F4/80+iNOS+) following D-lip/CM@GM treatment (Fig. 5 C, D and S7A, B), thereby substantiating that D-lip/CM@GM's potential to mitigate macrophage inflammation. Nuclear factor-kB (NF-kB) translocation plays a critical role in inflammation and macrophage glycolysis [41]. Through immunofluorescence, we found that D-lip/CM@GM could inhibit the translocation of macrophage p65 into the nucleus, effectively suppressed inflammation within macrophages (Fig. 5E, F). These findings imply that D-lip/CM@GM could potentially reduce inflammation through both GAPDH and NF-κB signaling pathways. Following D-lip/CM@GM posttreatment, the proinflammatory gene expression of iNOS, IL-1β, IL-6 and TNF-α was inhibited (Fig. 5G). Additionally, the treatment with D-lip/CM@GM resulted in the inhibition of iNOS and IL-1β expression (Figure. S8A, B). These findings suggest that glycolysis significantly contributes to the generation of proinflammatory cytokines and chemokines during the innate immune response. Our study confirmed that D-lip/CM@GM targets GAPDH, a key enzyme in glycolysis, and reduces the production of proinflammatory cytokines and chemokines by inhibiting the NF-κB signaling pathways and promoting macrophage transition (Fig. 5H).

Antibacterial properties of D-lip/CM@GM in vitro

Infection represents a severe complication of DIBD, necessitating multiple surgeries and long-term antibiotic treatment. This often results in soft tissue infections, delayed bone healing, amputations, and even death. Due to immune cell dysfunction and local hyperglycaemia, planktonic bacteria can settle and form biofilms to resist antibiotics upon entering bone defect sites [42]. Additionally, they can enter macrophages to become intracellular bacteria, evading destruction [43]. To thoroughly eradicate infection in the area of bone defect, extermination of planktonic bacteria, biofilms, and intracellular bacteria is indispensable.

S. *aureus* is the predominant pathogen associated with orthopedic procedures. The rise in antimicrobial resistance has made MRSA infections the primary cause of bone infection, presenting a significant challenge in managing this disease [44]. The prevalence of MRSA has resulted in significant morbidity and mortality, posing a major public health challenge [45]. Therefore, MRSA was selected as the experimental template.

The antibacterial ability was first tested via Live/Dead staining and blood agar plate experiments. As indicated in Fig. 6A, D-lip/CM@GM showed the potency to inhibit the growth of MRSA. These experimental observations are further affirmed by statistical analysis (Fig. 6B). Based on previous studies, we hypothesized that D-lip/CM@GM might suppress bacterial proliferation by specifically targeting GAPDH in MRSA [12]. Analysis on sequence homology divulged that the catalytic cysteine present in the active site of GAPDH, which is directly inhibited by DMF [12], bears notable sequence homology in human, mice and bacteria (Fig. 6D). Research has posited a crucial role for GAPDH in the constitution of bacterial biofilms [46]. Through 3D reconstruction, we discerned thinning biofilms and significant bacterial death after D-lip/CM@GM treatment (Fig. 6 C). MRSA could adjust to the glutamate surplus in the infected tissues by stimulating both glycolysis and aspartate biosynthesis - crucial pathways for its survival in such an environment. Specifically, glycolysis is vital for *S. aureus* survival [47, 48]. This suggests that DMF, which is akin to a nectar for inflammatory state macrophages, metamorphoses into a poison that threatens the survival of MRSA. We verified that D-lip/CM@GM directly suppressed GAPDH activity and decreased lactate secretion generated through glycolysis in MRSA (Fig.S9A, B). The destruction of the MRSA structure under the influence of D-lip/CM@GM was further attested by TEM (Fig. 6E). Aside from the aforementioned functions, D-lip/CM@GM could influence inflammatory macrophages, releasing internal D-lip to exert glycolysis suppression and eliminate intracellular bacteria (Fig. 6F). After constructing the intracellular bacteria model, we observed efficient MRSA eradication within macrophages via D-lip/CM@GM (Fig. 6G, H). These results instil confidence and support in treating bone defect infections. Different from conventional antibiotics, DMF is yet to breed resistance in multiple bacteria, thus performing better in diabetic patients prone to multi-infections and multi-drug-resistant bacterial infections. Diabetic feet are also victims of infection, hence future research should further expand the application scope of this material.

Therapeutic efficacy of D-lip/CM@GM on bone reconstruction in vivo

We further constructed the DIBD rat model to evaluate the therapeutic effect of D-lip/CM@GM hydrogel (Fig. 7A). Diabetic rats were anesthetized, and a 2 mm diameter bone defect was drilled into the femoral condyle. MRSA was then introduced to establish a diabetic infectious bone defect model (Fig. 7B). Seven days post-implantation, we observed clear infection

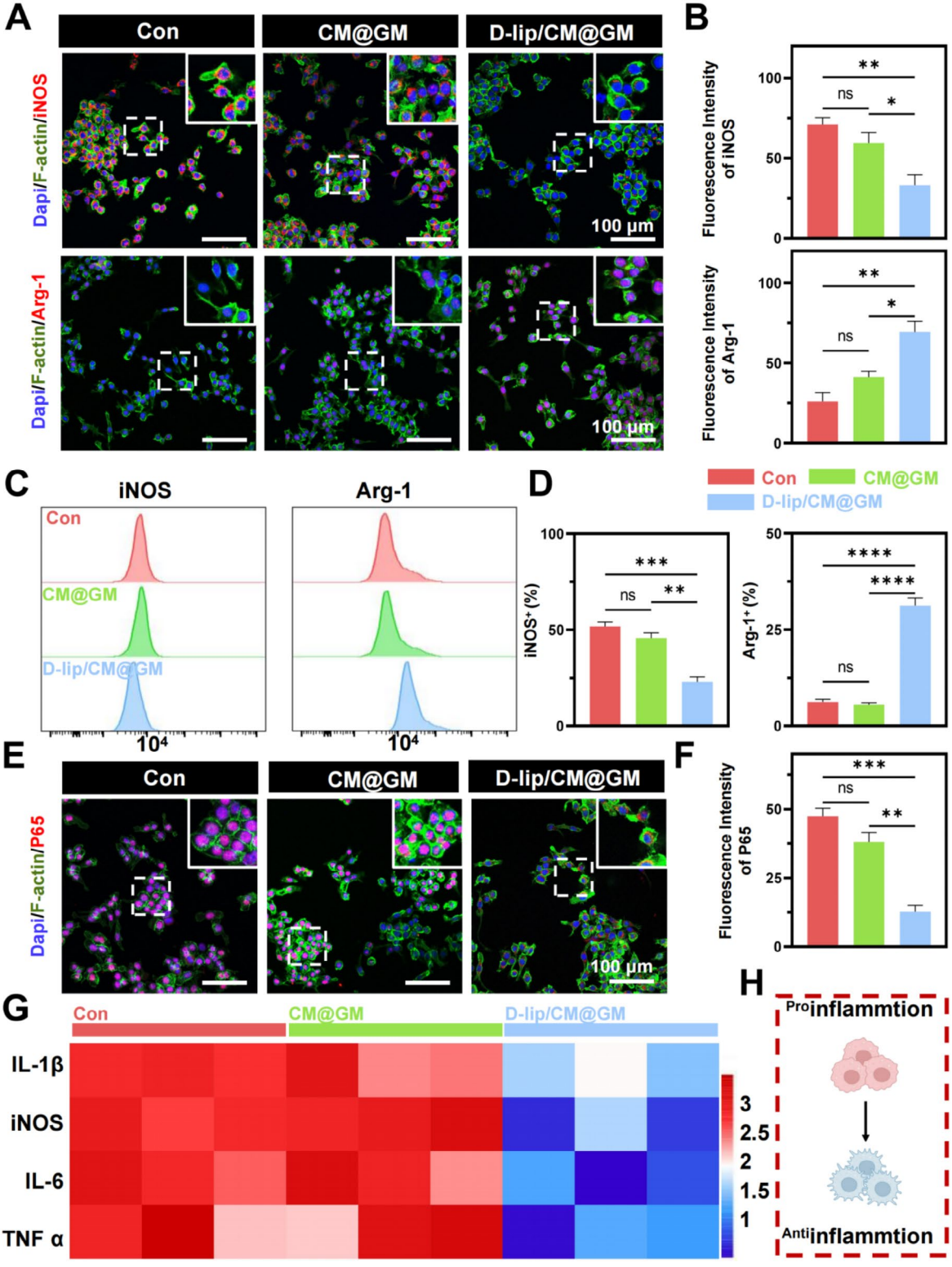

Fig. 5 D-lip/CM@GM can regulate inflammatory responses in macrophages. (**A**). Representative immunofluorescence staining of iNOS and Arg-1 in macrophages. (**B**). Quantitative analysis of iNOS and Arg-1 in different treatment groups. (**C**). Flow cytometry of iNOS and Arg-1 in macrophages. (**D**). Quantitative analysis of $iNOS^+$ and $Arg\text{-}1^+$ in the different treatment groups. (**E**). Representative immunofluorescence staining of p65 (Red) and F-actin (Green) in macrophages. (**F**). Quantitative analysis of p65 in the different treatment groups. (**G**). RNA levels of IL-1β, iNOS, IL-6 and TNF α in macrophages were determined using RT-PCR. (**H**). D-lip/CM@GM can promote macrophages transition. The values represent mean ± SD. Statistically significant differences are indicated as ns where $p \geq 0.05$, * where $p < 0.05$, ** where $p < 0.01$, *** where $p < 0.001$, and **** where $p < 0.0001$ between the indicated groups

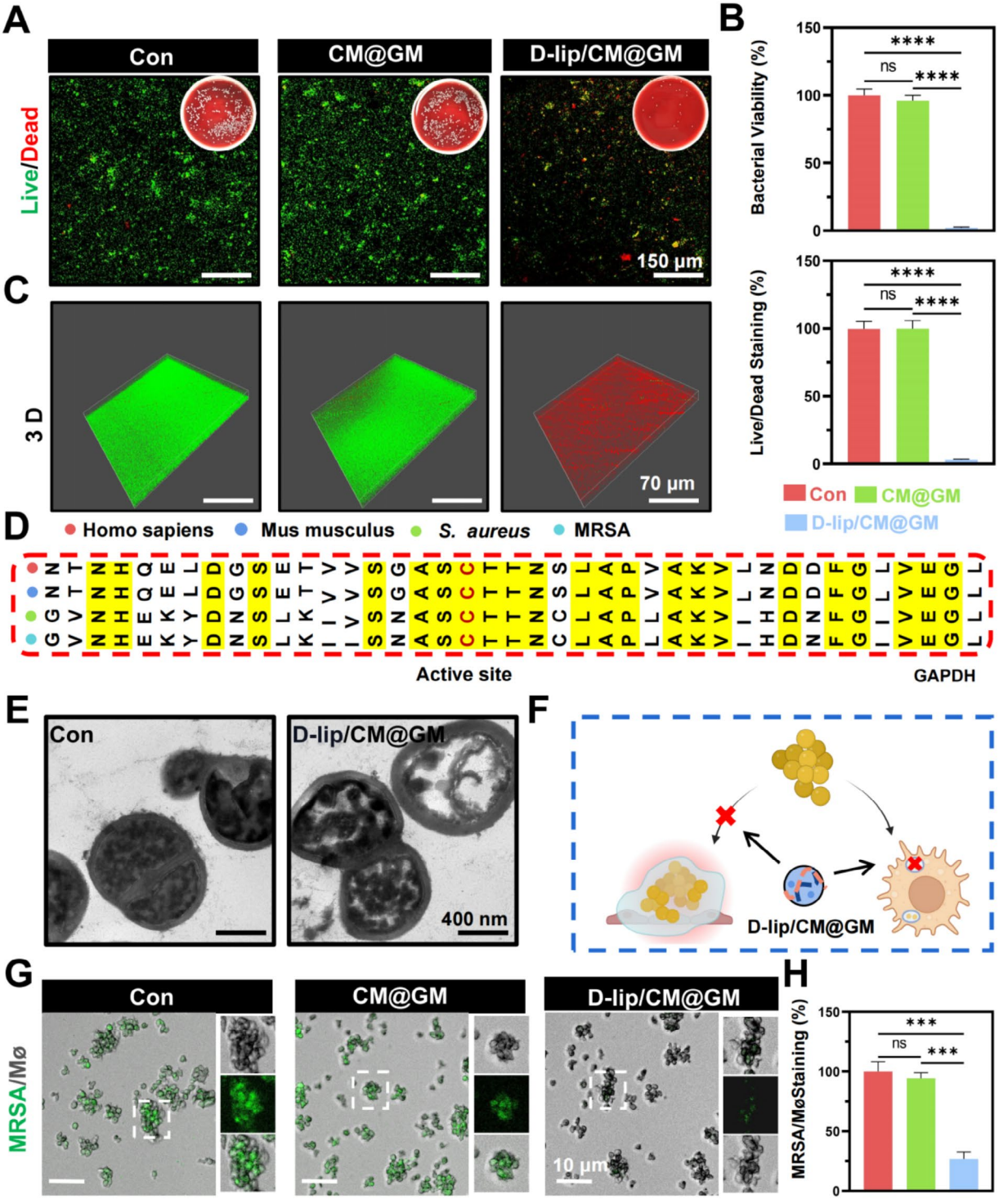

Fig. 6 Antibacterial properties of D-lip/CM@GM in vitro. (**A**). Antibacterial properties of D-lip/CM@GM in MRSA via standard plate counting method in blood agar plate and Live/Dead staining. (**B**). Quantitative analysis of bacterial viability and Live/Dead staining ratio in MRSA under the treatment of the different groups. (**C**). 3D reconstruction showcasing the Live/Dead staining of the bacterial biofilm in different groups. (**D**). The alignment of the GAPDH amino acid sequence in Homo sapiens, Mus musculus, *S. aureus*, and MRSA252. The active cysteine site is indicated by the highlighted red portion. (**E**). Representative TEM micrographs showing MRSA morphology after treatment with D-lip/CM@GM. (**F**). Schematic showing that D-lip/CM@GM suppresses both extra- and intracellular growth of MRSA, as well as its biofilm formation. (**G**). Representative images of Green fluorescent protein (GFP) -MRSA in macrophage at 4 h. (**H**). Semi-quantitative analysis of MRSA in macrophage compared to the control group. The values represent mean ± SD. Statistically, significant differences are indicated as ns where $p \geq 0.05$, * where $p < 0.05$, ** where $p < 0.01$, *** where $p < 0.001$, and **** where $p < 0.0001$ between the indicated groups

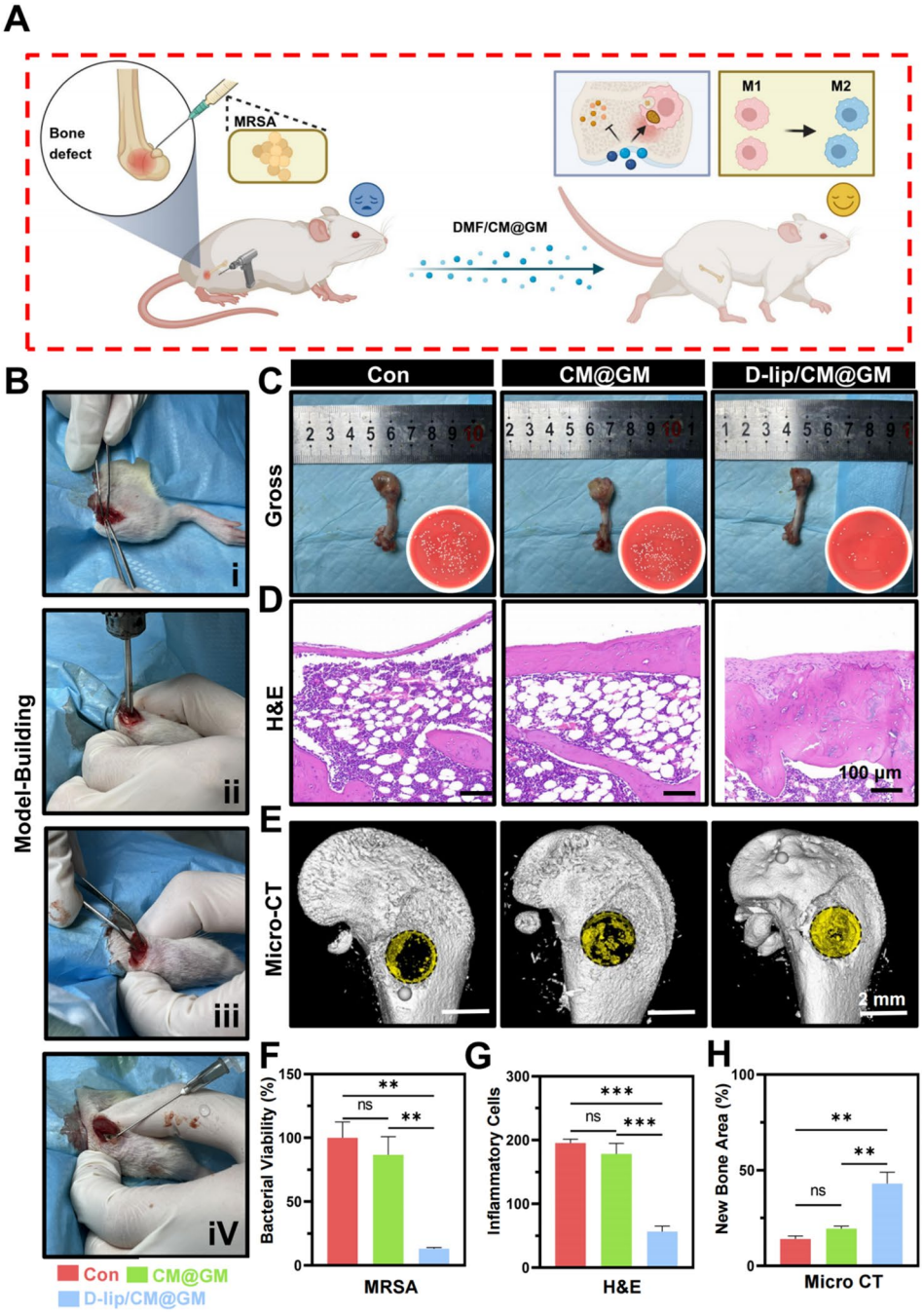

Fig. 7 Therapeutic Efficacy of D-lip/CM@GM on DIBD. (**A**). Schematic of preparing the DIBD model and collection. (**B**). Process of DIBD model establishment, including (i) cut open, (ii) drilling a hole, (iii) exposure of the defect area and (iv) incubating MRSA and microsphere. (**C**). Representative gross images and bacterial counts of MRSA of local infection in the bone tissues. (**D**). H&E staining about inflammatory responses in different groups. (**E**). Representative micro-CT images of bone defects treated with different groups. The yellow area represents the bone defect location. (**F**). Quantitative analysis of the bacterial viability with different groups. (**G**). Quantitative analysis of the inflammatory cells treated with different groups. (**H**). Quantitative analysis of the new bone area treated with different groups. The values represent mean ± SD. Statistically, significant differences are indicated as ns where $p \geq 0.05$, * where $p < 0.05$, ** where $p < 0.01$, *** where $p < 0.001$, and **** where $p < 0.0001$ between the indicated groups

and tissue deformation in the femurs treated with pure CM@GM, while no significant changes were noted in the femurs of the CM@GM and D-lip/CM@GM groups (Fig. 7 C). After four weeks, bacteria extracted from the tissues and cultivated on a blood agar plate show that MRSA in the defect and CM@GM groups were significantly higher than the other two groups (Fig. 7 C, F). The results indicate that bacterial

levels were significantly reduced in the D-lip/CM@GM treatment group, suggesting effective infection control. Infection control is crucial in treating diabetic infectious bone defects since it exacerbates the local inflammatory microenvironment and disrupts tissue regeneration. The results show that D-lip/CM@GM can effectively kill intra-tissue bacteria creating favorable conditions for bone defect healing. Subsequently, the impact of D-lip/CM@GM on bone regeneration was analyzed through histological and radiological examinations. H&E staining showed severe inflammation in the defect and the CM@GM groups, while reduced inflammation was observed in the D-lip/CM@GM group (Fig. 7D). The statistical analysis reveals that the D-lip/CM@GM group exerts a suppressive effect on inflammatory response (Fig. 7G). Moreover, micro-CT results revealed extensive bone defect areas in the defect and CM@GM groups due to bacterial erosion of the epiphysis. In contrast, the D-lip/CM@GM group showed significant new bone formation (Fig. 7E). The bone volume/total volume (BV/TV) ratio of D-lip/CM@GM was also significantly higher than the other groups (Fig. 7H).

Additionally, we further investigated in vivo immune cell inflammation activation and specific metabolic changes. The results show that the iNOS expression was significantly lower than the other groups, while the Arg-1 expression was significantly higher than the other two groups (Fig. 8A, D). Furthermore, p-P65 positive expression was observed in the bone destruction area (Fig. 8B), which is considered a crucial factor in NF-κB activation and plays a pivotal role in macrophage glycolysis [49]. Previous in vitro studies have demonstrated that D-lip/CM@GM can affect and reduce the expression of NF-κB-related signaling pathways. The lowest p-P65 expression was observed

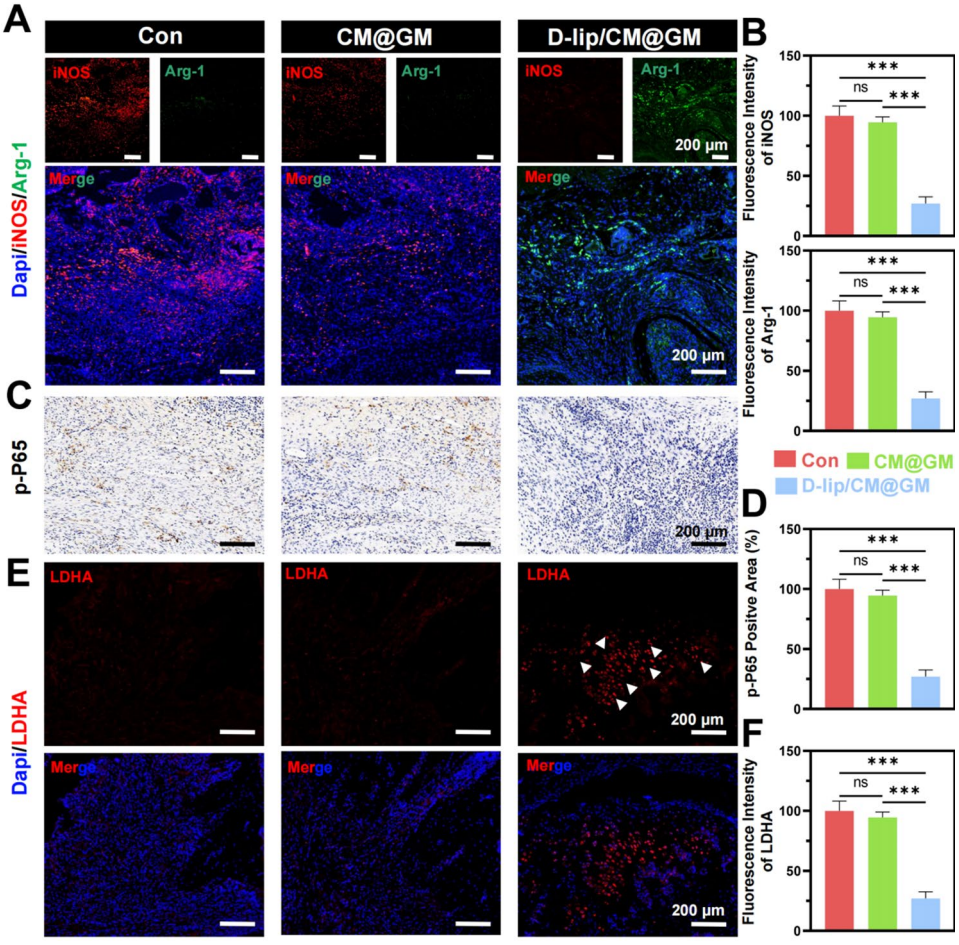

Fig. 8 Immunofluorescence and immunohistochemical staining of bone tissues. (**A**). Representative immunofluorescence staining images of iNOS (Red) and Arg-1 (Green) in bone defect. (**B**). Relative fluorescence intensity of iNOS and Arg-1 in different group. (**C**). Representative immunohistochemical staining of p-P65 in bone defect. (**D**). Quantitative analysis of p-P65 positive area in different groups. (**E**). Representative immunofluorescence staining images of LDHA (Red) in bone defect. (**F**). Relative fluorescence intensity of LDHA in different groups. The values represent mean ± SD. Statistically, significant differences are indicated as ns where $p \geq 0.05$, * where $p < 0.05$, ** where $p < 0.01$, *** where $p < 0.001$, and **** where $p < 0.0001$ between the indicated groups

in D-lip/CM@GM group, indicating that this hydrogel can inhibit the expression of NF-κB in macrophages (Fig. 8B, E). With GAPDH inhibition, there may be an elevation in the expression of Lactate dehydrogenase A (LDHA), the enzyme that catalyzes the conversion of pyruvate to lactate in the glycolytic pathway. This elevation could potentially assist the polarization of macrophages towards an anti-inflammatory phenotype [50]. Expression levels in the D-lip/CM@GM group were higher than those in other groups (Fig. 8C, F). In conclusion, these results suggest that the D-lip/CM@GM hydrogel exhibited the most effective bone repair effect in the diabetic infection bone defect model, owing to its antibacterial features, immune environment reconstruction, and osteogenic differentiation promotion.

Conclusion

In this study, an injectable, macrophage-modulated 'GAPDH-Silence' microsphere as a composite drug delivery system was developed with the aim to reprogram macrophage metabolism and eradicate bacteria. This microsphere, with collagenase-responsive properties, allows for on-demand release, quickly elevating the concentration of drug agents at the infected site, thereby boosting treatment efficacy. In vitro results showed antibacterial, immune regulation and metabolism reprogramming of the GAPDH-Silence microsphere system. In the MRSA-infected DIBD model, the D-lip/CM@GM hydrogel was proven effective in helping bone regeneration and reducing the severity of bacterial infection. Overall, we expect that such a GAPDH-Silence microsphere system would provide a useful strategy for both metabolism-based therapies and bone defect treatment.

Supplementary Information

The online version contains supplementary material available at https://doi.org/10.1186/s12951-024-02787-9.

Supplementary Material 1

Acknowledgements

We thank help from Biorender (BioRender). We thank the excellent technical assistant of Xingguang Liang and Fangjie Lu from microscopy core facility, Central Laboratory, the First Affiliated Hospital, Zhejiang University School of Medicine with the confocal laser microscopy.

Author contributions

Pengfei Lei, Yihe Hu, and Yong Zhang designed the research; Jiale Jin, Xiaowei Xia, and Yiqi Yang conducted the experiments in vivo and in vitro; Dongdong Li, Zhiyuan Luo prepared the figures; Dongyu Wang collected the samples and assessed the outcomes; Jiale Jin and Yifang Qin analyzed the data; Chengxin Ruan and Jiale Jin wrote the paper. All authors contributed to the article and approved the submitted version.

Funding

This study was supported by the Key Research and Development Program of Hunan Province (Grant No. 2020SK2008 and 2021GK2012), the Major Science and Technology Projects of Changsha City (Grant No. kh2003016), the Natural Science Foundation Exploration Project of Zhejiang Province, China (Grant No. Y23H060040), the Medical and Health Research Project of Zhejiang Province (2024KY986 and 2023KY098), the Natural Science Foundation of Hunan Province, China (Grant No. 2022JJ30934), National Key Research and Development Program of China (2023YFC2412604 and 2023YFC2412605), and the Zhejiang Province Leading Geese Plan (2024C03079).

Data availability

All the data necessary for evaluating the conclusions in the paper can be found in the paper itself or in the Supplementary Materials.

Declarations

Ethics approval and consent to participate

The rat experiment received ethical approval from the Animal Experimental Ethical Inspection of the First Affiliated Hospital, Zhejiang University School of Medicine, with the approval number 2024sydw1252.

Consent for publication

All of our authors agree to be published.

Competing interests

All authors have declared that they do not have any competing interests.

Received: 19 June 2024 / Accepted: 18 August 2024
Published online: 29 August 2024

References

1. Hamann C, Kirschner S, Gunther KP, Hofbauer LC. Bone, sweet bone–osteoporotic fractures in diabetes mellitus. Nat Rev Endocrinol. 2012;8:297–305.
2. He M, Wang H, Han Q, Shi X, He S, Sun J, Zhu Z, Gan X, Deng Y. Glucose-primed PEEK orthopedic implants for antibacterial therapy and safeguarding diabetic osseointegration. Biomaterials. 2023;303:122355.
3. Levin-Reisman I, Ronin I, Gefen O, Braniss I, Shoresh N, Balaban NQ. Antibiotic tolerance facilitates the evolution of resistance. Science. 2017;355:826–30.
4. Li J, Li K, Du Y, Tang X, Liu C, Cao S, Zhao B, Huang H, Zhao H, Kong W, et al. Dual-nozzle 3D printed Nano-Hydroxyapatite Scaffold loaded with Vancomycin sustained-release microspheres for enhancing bone regeneration. Int J Nanomed. 2023;18:307–22.
5. Brereton MF, Rohm M, Shimomura K, Holland C, Tornovsky-Babeay S, Dadon D, Iberl M, Chibalina MV, Lee S, Glaser B, et al. Hyperglycaemia induces metabolic dysfunction and glycogen accumulation in pancreatic β-cells. Nat Commun. 2016;7:13496.
6. Russo S, Kwiatkowski M, Govorukhina N, Bischoff R, Melgert BN. Meta-inflammation and metabolic reprogramming of macrophages in diabetes and obesity: the importance of metabolites. Front Immunol. 2021;12:746151.
7. Eizirik DL, Pasquali L, Cnop M. Pancreatic β-cells in type 1 and type 2 diabetes mellitus: different pathways to failure. Nat Rev Endocrinol. 2020;16:349–62.
8. Qian H, Lei T, Hua L, Zhang Y, Wang D, Nan J, Liu W, Sun Y, Hu Y, Lei P. Fabrication, bacteriostasis and osteointegration properties researches of the additively-manufactured porous tantalum scaffolds loading Vancomycin. Bioact Mater. 2023;24:450–62.
9. Zheng Z, Yin W, Zara JN, Li W, Kwak J, Mamidi R, Lee M, Siu RK, Ngo R, Wang J, et al. The use of BMP-2 coupled - Nanosilver-PLGA composite grafts to induce bone repair in grossly infected segmental defects. Biomaterials. 2010;31:9293–300.
10. Zhou W, Bai T, Wang L, Cheng Y, Xia D, Yu S, Zheng Y. Biomimetic AgNPs@antimicrobial peptide/silk fibroin coating for infection-trigger antibacterial capability and enhanced osseointegration. Bioact Mater. 2023;20:64–80.
11. Ouyang L, Chen B, Liu X, Wang D, Li Y, Liao Y, Yeung KWK, Liu X. Puerarin@Chitosan composite for infected bone repair through mimicking the biofunctions of antimicrobial peptides. Bioact Mater. 2023;21:520–30.
12. Kwon HK, Yu KE, Cahill SV, Alder KD, Dussik CM, Kim SH, Sharma L, Back J, Oh I, Lee FY. Concurrent targeting of glycolysis in bacteria and host cell inflammation in septic arthritis. EMBO Mol Med. 2022;14:e15284.

13. Wherry EJ, Kurachi M. Molecular and cellular insights into T cell exhaustion. Nat Rev Immunol. 2015;15:486–99.
14. Sun P, Cui M, Jing J, Kong F, Wang S, Tang L, Leng J, Chen K. Deciphering the molecular and cellular atlas of immune cells in septic patients with different bacterial infections. J Transl Med. 2023;21:777.
15. Kornberg MD, Bhargava P, Kim PM, Putluri V, Snowman AM, Putluri N, Calabresi PA, Snyder SH. Dimethyl fumarate targets GAPDH and aerobic glycolysis to modulate immunity. Science. 2018;360:449–53.
16. Wang X, Fu SQ, Yuan X, Yu F, Ji Q, Tang HW, Li RK, Huang S, Huang PQ, Qin WT, et al. A GAPDH serotonylation system couples CD8(+) T cell glycolytic metabolism to antitumor immunity. Mol Cell. 2024;84:760–e775767.
17. Liao ST, Han C, Xu DQ, Fu XW, Wang JS, Kong LY. 4-Octyl itaconate inhibits aerobic glycolysis by targeting GAPDH to exert anti-inflammatory effects. Nat Commun. 2019;10:5091.
18. Nicolay JP, Müller-Decker K, Schroeder A, Brechmann M, Möbs M, Géraud C, Assaf C, Goerdt S, Krammer PH, Gülow K. Dimethyl fumarate restores apoptosis sensitivity and inhibits tumor growth and metastasis in CTCL by targeting NF-κB. Blood. 2016;128:805–15.
19. Dello Russo C, Scott KA, Pirmohamed M. Dimethyl fumarate induced Lymphopenia in multiple sclerosis: a review of the literature. Pharmacol Ther. 2021;219:107710.
20. Jin J, Liu Y, Jiang C, Shen Y, Chu G, Liu C, Jiang L, Huang G, Qin Y, Zhang Y, et al. Arbutin-modified microspheres prevent osteoarthritis progression by mobilizing local anti-inflammatory and antioxidant responses. Mater Today Bio. 2022;16:100370.
21. Zhou B, Jiang X, Zhou X, Tan W, Luo H, Lei S, Yang Y. GelMA-based bioactive hydrogel scaffolds with multiple bone defect repair functions: therapeutic strategies and recent advances. Biomater Res. 2023;27:86.
22. Li K, Ju X, Li X, Lu G, Ou J, Xu D, Wan C, Zhu M, Du C, Tian Y, Niu Z. In situ formed antibacterial hydrogel with collagenase-responsive activity for prevention of MRSA-induced osteomyelitis. Chem Eng J. 2024;489:151475.
23. Hochberg MC, Martel-Pelletier J, Monfort J, Möller I, Castillo JR, Arden N, Berenbaum F, Blanco FJ, Conaghan PG, Doménech G, et al. Combined chondroitin sulfate and glucosamine for painful knee osteoarthritis: a multicentre, randomised, double-blind, non-inferiority trial versus celecoxib. Ann Rheum Dis. 2016;75:37–44.
24. He Y, Sun M, Wang J, Yang X, Lin C, Ge L, Ying C, Xu K, Liu A, Wu L. Chondroitin sulfate microspheres anchored with drug-loaded liposomes play a dual antioxidant role in the treatment of osteoarthritis. Acta Biomater. 2022;151:512–27.
25. Li Y, Hou H, Liu Z, Tang W, Wang J, Lu L, Fu J, Gao D, Zhao F, Gao X, et al. CD44 targeting nanodrug based on chondroitin sulfate for melanoma therapy by inducing mitochondrial apoptosis pathways. Carbohydr Polym. 2023;320:121255.
26. Liu S, Liu Z, Shang A, Xun J, Lv Z, Zhou S, Liu C, Zhang Q, Yang Y. CD44 is a potential immunotherapeutic target and affects macrophage infiltration leading to poor prognosis. Sci Rep. 2023;13:9657.
27. Wang Y, Bryant SH, Cheng T, Wang J, Gindulyte A, Shoemaker BA, Thiessen PA, He S, Zhang J. PubChem BioAssay: 2017 update. Nucleic Acids Res. 2017;45:D955–63.
28. Xiao S, Zhao T, Wang J, Wang C, Du J, Ying L, Lin J, Zhang C, Hu W, Wang L, Xu K. Gelatin methacrylate (GelMA)-Based hydrogels for cell transplantation: an effective strategy for tissue Engineering. Stem Cell Rev Rep. 2019;15:664–79.
29. Han Y, Yang J, Zhao W, Wang H, Sun Y, Chen Y, Luo J, Deng L, Xu X, Cui W, Zhang H. Biomimetic injectable hydrogel microspheres with enhanced lubrication and controllable drug release for the treatment of osteoarthritis. Bioact Mater. 2021;6:3596–607.
30. Nazir F, Ashraf I, Iqbal M, Ahmad T, Anjum S. 6-deoxy-aminocellulose derivatives embedded soft gelatin methacryloyl (GelMA) hydrogels for improved wound healing applications: in vitro and in vivo studies. Int J Biol Macromol. 2021;185:419–33.
31. Xiao P, Han X, Huang Y, Yang J, Chen L, Cai Z, Hu N, Cui W, Huang W. Reprogramming macrophages via immune cell mobilized hydrogel microspheres for osteoarthritis treatments. Bioact Mater. 2024;32:242–59.
32. Lu HT, Chang WT, Tsai ML, Chen CH, Chen WY, Mi FL. Development of Injectable Fucoidan and Biological macromolecules Hybrid Hydrogels for Intra-articular Delivery of platelet-rich plasma. Mar Drugs 2019, 17.
33. Ai C, Liu L, Wong K, Tan XH, Goh JCH. The effect of chondroitin sulfate concentration and matrix stiffness on chondrogenic differentiation of mesenchymal stem cells. Biomater Sci. 2023;11:4557–73.
34. Xu K, Yang H, Fang J, Qiu K, Shen H, Huang G, Zheng Q, Wang C, Xu T, Yu X, et al. Self-adaptive pyroptosis-responsive nanoliposomes block pyroptosis in autoimmune inflammatory diseases. Bioact Mater. 2024;36:272–86.
35. Liu J, Wu Z, Liu Y, Zhan Z, Yang L, Wang C, Jiang Q, Ran H, Li P, Wang Z. ROS-responsive liposomes as an inhaled drug delivery nanoplatform for idiopathic pulmonary fibrosis treatment via Nrf2 signaling. J Nanobiotechnol. 2022;20:213.
36. Yarana C, Thompson H, Chaiswing L, Butterfield DA, Weiss H, Bondada S, Alhakeem S, Sukati S. St Clair DK: extracellular vesicle-mediated macrophage activation: an insight into the mechanism of thioredoxin-mediated immune activation. Redox Biol. 2019;26:101237.
37. Zhang H, Chen T, Ren J, Xia Y, Onuma A, Wang Y, He J, Wu J, Wang H, Hamad A, et al. Pre-operative exercise therapy triggers anti-inflammatory trained immunity of Kupffer cells through metabolic reprogramming. Nat Metab. 2021;3:843–58.
38. Odegaard JI, Chawla A. Alternative macrophage activation and metabolism. Annu Rev Pathol. 2011;6:275–97.
39. Thiem K, Keating ST, Netea MG, Riksen NP, Tack CJ, van Diepen J, Stienstra R. Hyperglycemic memory of Innate Immune cells promotes in Vitro Proinflammatory responses of human monocytes and Murine Macrophages. J Immunol. 2021;206:807–13.
40. Zhang K, Sun W, Huang L, Zhu K, Pei F, Zhu L, Wang Q, Lu Y, Zhang H, Jin H, et al. Identifying glyceraldehyde 3-Phosphate dehydrogenase as a cyclic Adenosine Diphosphoribose binding protein by photoaffinity protein-ligand labeling Approach. J Am Chem Soc. 2017;139:156–70.
41. Guo D, Tong Y, Jiang X, Meng Y, Jiang H, Du L, Wu Q, Li S, Luo S, Li M, et al. Aerobic glycolysis promotes tumor immune evasion by hexokinase2-mediated phosphorylation of IκBα. Cell Metab. 2022;34:1312–e13241316.
42. Li B, Shu R, Dai W, Yang F, Xu H, Shi X, Li Y, Bai D, Yang W, Deng Y. Bioheterojunction-Engineered Polyetheretherketone Implants with Diabetic Infectious Micromilieu Twin-Engine Powered Disinfection for Boosted Osteogenicity. Small. 2022;18:e2203619.
43. Hodgson K, Morris J, Bridson T, Govan B, Rush C, Ketheesan N. Immunological mechanisms contributing to the double burden of diabetes and intracellular bacterial infections. Immunology. 2015;144:171–85.
44. Turner NA, Sharma-Kuinkel BK, Maskarinec SA, Eichenberger EM, Shah PP, Carugati M, Holland TL, Fowler VG Jr. Methicillin-resistant Staphylococcus aureus: an overview of basic and clinical research. Nat Rev Microbiol. 2019;17:203–18.
45. Osmundson J, Montero-Diez C, Westblade LF, Hochschild A, Darst SA. Promoter-specific transcription inhibition in Staphylococcus aureus by a phage protein. Cell. 2012;151:1005–16.
46. Kang XM, Wang FF, Zhang H, Zhang Q, Qiana W. Genome-wide identification of genes necessary for biofilm formation by nosocomial pathogen Stenotrophomonas maltophilia reveals that orphan response regulator FsnR is a critical modulator. Appl Environ Microbiol. 2015;81:1200–9.
47. Wong Fok Lung T, Monk IR, Acker KP, Mu A, Wang N, Riquelme SA, Pires S, Noguera LP, Dach F, Gabryszewski SJ, et al. Staphylococcus aureus small colony variants impair host immunity by activating host cell glycolysis and inducing necroptosis. Nat Microbiol. 2020;5:141–53.
48. Prince A, Wong Fok Lung T. Consequences of metabolic interactions during Staphylococcus aureus infection. Toxins (Basel) 2020, 12.
49. Morrissey SM, Zhang F, Ding C, Montoya-Durango DE, Hu X, Yang C, Wang Z, Yuan F, Fox M, Zhang HG et al. Tumor-derived exosomes drive immunosuppressive macrophages in a pre-metastatic niche through glycolytic dominant metabolic reprogramming. *Cell Metab* 2021, 33:2040–2058.e2010.
50. Chen Y, Wu G, Li M, Hesse M, Ma Y, Chen W, Huang H, Liu Y, Xu W, Tang Y, et al. LDHA-mediated metabolic reprogramming promoted cardiomyocyte proliferation by alleviating ROS and inducing M2 macrophage polarization. Redox Biol. 2022;56:102446.

Publisher's note